Roles of chalcogen sublayers of 1*H* transition metal dichalcogenides in metal-semiconductor van der Waals heterostructures

Tetsuro Habe
Nagamori Institute of Actuators, Kyoto University of Advanced Science, Kyoto 615-8577, Japan

(Received 11 September 2023; revised 2 February 2024; accepted 6 February 2024; published 28 February 2024)

In this paper, the crystal and electronic structures are investigated using first-principles theory for metal-semiconductor van der Waals heterostructures 1*H*-transition-metal dichalcogenides (NbS_2, $NbSe_2$, TaS_2, $TaSe_2$, MoS_2, $MoSe_2$, WS_2, and WSe_2). The theoretical investigations reveal that chalcogen sublayers play crucial roles in the crystal and electronic structures though these sublayers are minor parts in the pristine crystals. Actually, selenide sublayers energetically stabilize the commensurate heterobilayers, whereas moiré structure gives a much lower electronic energy with sulfide sublayers. Moreover, the chalcogen sublayers dominate the charge distribution via the difference of work functions in the component layers, i.e., the charge transfer between the metallic and semiconducting layers in the heterobilayers. The theoretical results suggest that the chalcogen sublayers can be the key to control the crystal and electronic structures in the metal-semiconductor vdW heterostructure of TMDC monolayers.

DOI: 10.1103/PhysRevB.109.075308

I. INTRODUCTION

The electronic properties of pristine transition-metal dichalcogenides (TMDCs) of group-V and -VI atoms are mainly dominated by transition metal [1–6]. These TMDCs are atomic layered materials, which are composed of thin layerlike crystals stacked vertically with van der Waals interaction. Each layer also consists of three sublayers: the top and bottom chalcogen sublayers and middle transition-metal sublayer, strongly bonded to each other [7]. The group-V and -VI transition-metal sublayers lead to the metallic and semiconducting properties, respectively, in the atomic layered materials. On the other hand, the effect of the chalcogen sublayers is limited to small variations in the energy dispersion, the band gap, and the lattice constant for the pristine monolayer, multilayer, and bulk crystal except for Janus structure [8,9] breaking the crystal symmetry.

In heterostructures of semiconducting TMDC monolayers, the chalcogen sublayers play a slightly important role in terms of the lattice structure due to the effect of the chalcogen on the lattice constant. In the case of multilayer of different layerlike crystals, the so-called van der Waals (vdW) heteromultilayer [10–13], the lattice structure can be commensurate only if the component layers possess the same lattice constant [14,15]. In other words, the commensurate vdW heterostructures lead the component layers to be expanded or compressed to match their lattice constants with each other as shown in Fig. 1. Otherwise, multilayers have moiré structures, where the periodicity is absent or much larger than that of each layer [16–19]. Since TMDCs of transition metals in the same group possess comparable lattice constants with the same chalcogen, the semiconducting monolayers can form a commensurate vdW heteromultilayer and thus preserve the valley structure, one of the most important features of TMDCs, in the reciprocal space.

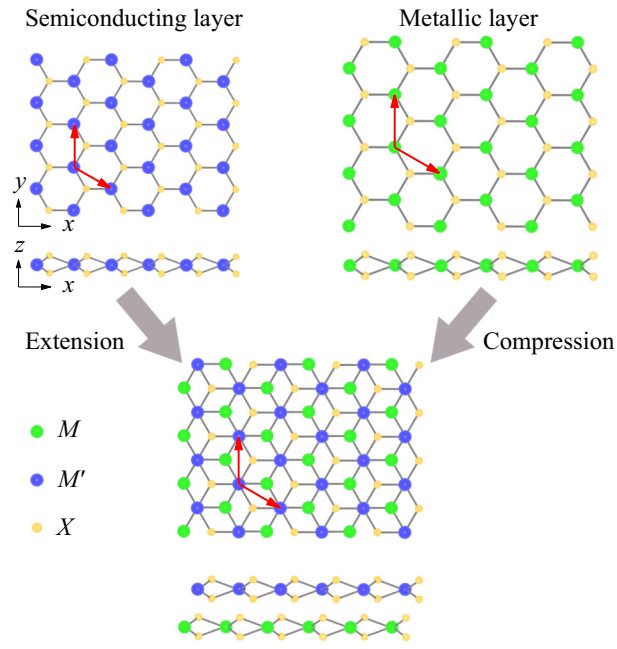

FIG. 1. Schematic of a commensurate heterobilayer consisting of two monolayers with different lattice constants. Each layered material is drawn in the top and horizontal point of view. Two arrows on each top view represent the lattice vectors of the two dimensional lattice structure.

Recently, the heterostructures have been extended to combinations of metallic and semiconducting TMDCs, i.e., those with transition metals in group V and VI, respectively. For in-plane junctions, so-called lateral heterojunctions, the interface between two layers can be an atomically commensurate structure stabilized by the strong intralayer atomic bond. In practice, the commensurate interface had been experimentally observed [20] and thus this condition is assumed in the theoretical works [21–23]. For vdW heterostructures, on the other hand, the commensurate alignment between the component layers cannot be expected due to the interlayer interaction being much weaker than the intralayer bonding. In practice, a vdW heterostructure of NbS_2 and MoS_2 fabricated using the chemical vapor deposition method possesses an incommensurate stacking structure, the so-called moiré pattern, with R-type orientation of the component layers [24]. However, the previous theoretical works [25,26] adopted the commensurate alignment for the stacking and did not apply the R-type orientation. On the other hand, in a previous theoretical work [27], the stable stacking structure of NbS_2 and $MoSe_2$ is theoretically investigated and predicted to be an R-type commensurate stacking, $2R_2$, as the stable structure. The theoretical prediction for R-type orientation is consistent with the experimental work [24] but the commensurate stacking had not been observed in the case of NbS_2 and MoS_2 heterostructure. Thus the previous experimental and theoretical works imply that the stacking structure of metal-semiconductor heterostructure of TMDCs is affected by the chalcogen elements in the component layers.

In this paper, we investigate the stability of commensurate heterostructures of group-V and -VI TMDC monolayers with the same chalcogen as shown in Fig. 1 and the electronic structures in the heterobilayers. In Sec. II, the stability of these heterostructures is theoretically evaluated with first-principles calculations for the lattice optimization and the energy variation under lattice compression or extension. The most stable stacking is revealed for the vdW heterostructures and also energetically compared with the moiré heterostructure. In Sec. III, the spinful electronic structures are presented for the most stable commensurate heterostructure. We reveal that the corrections for vdW interaction and spin-orbit coupling are necessary in different processes in a first-principles band calculation and that both the corrections can be incorporated for obtaining electronic structures. The difference between two cases of metal-semiconductor vdW heterostructures with a single chalcogen and with two chalcogens is also presented in terms of electronic structure. Moreover, the origin of the difference is revealed in terms of the effect of chalcogen on the work functions of the component layers. The conclusion is given in Sec. IV.

II. STABILITY OF COMMENSURATE HETEROSTRUCTURE

In this section, the feasible heterostructure is investigated for each combination of the metallic and semiconducting TMDC layers energetically using first-principles calculation with the effect of interlayer vdW interaction. In this work, honeycomb monolayer TMDCs ($1H$-TMDCs) are adopted as the component layers for the heterostructure and these layers are assumed to possess the same direction of honeycomb lattice as shown in Fig. 1. A monolayer TMDC consists of three sublayers, one transition-metal sublayer sandwiched by two chalcogen sublayers, that are strongly bonded to each other, and the layerlike crystals of the three sublayers are weakly bonded via vdW interaction in a heteromultilayer.

There are two possible stacking structures of vdW heterobilayer, commensurate, and moiré stacking structures. The two types of stacking structures minimize different components in the electronic energy. In the moiré structure, each component layer preserves the pristine lattice constant minimizing the deformation energy. On the other hand, the commensurate structure enforces the component layers to be deformed to match the lattice constant in the renewed honeycomb lattice. However, the commensurate stacking enhances the interlayer coupling in comparison with the incommensurate stacking, i.e., moiré structure, and reduces the electronic energy in terms of the interlayer coupling energy. If the contribution of the interlayer coupling is smaller than that of the lattice deformation, the heterostructure prefers a moiré structure of the layers with different lattice constants [16,17].

In this section, the stability of the commensurate vdW heterostructure and the role of the calcogen sublayers are investigated for combinations of MX_2 and $M'X_2$ with M = Nb or Ta, M' = Mo or W, and X = S or Se with a visible difference in the lattice constants.

The following first-principles calculations are performed using QUANTUM ESPRESSO [28], a package of numerical codes for density functional theory (DFT), with the Perdew-Burke-Emzerhof functional [29] in projector augmented wave method. For including effects of vdW interaction, a correction to the exchange-correlation (XC) functional, vdw-df-C6 [30], is applied to the calculations [31]. The correction reproduces the distance dependence of vdW interaction and it is employed except for the spinful calculations because the DFT calculations cannot include both effects of spin-orbit interaction and vdW interaction simultaneously. The energy cutoff is 60 Ry for the plane wave basis and 500 Ry for the charge density on a k mesh of $12 \times 12 \times 1$ in the first Brillouin zone. To simulate isolated monolayers or heterobilayers, the lattice constant 30 Å in the z axis, the perpendicular direction to the layers, is adopted for their unit cells. The convergence criterion is 10^{-8} Ry for the self-consistent field calculation. For lattice relaxation calculations, vc-relax in QUANTUM ESPRESSO is used with the correction for vdW interaction [32] and the convergence threshold is 10^{-2} kbar for stresses and 10^{-4} Ry/Bohr for forces. In all calculations for lattice relaxations, the lattice constant of the honeycomb lattice and the atomic positions in the z axis are optimized by this code except where specially noted.

First, the ground-state energy is investigated for several commensurate stacking structures to identify the lowest energy one. Four highly symmetric stacking patterns shown in Fig. 2 are considered as the candidates. Two of them, $2H_a$ and $2H_c$, include two inverted monolayers in which the positions of transition-metal and chalcogen atoms are exchanged in the honeycomb lattice. Here, the exchange of atoms leads to that of the K and K' points in the reciprocal space. The other two, $2R_1$ and $2R_2$, consist of two monolayers with the same order of these atoms. The numerical calculations are performed in

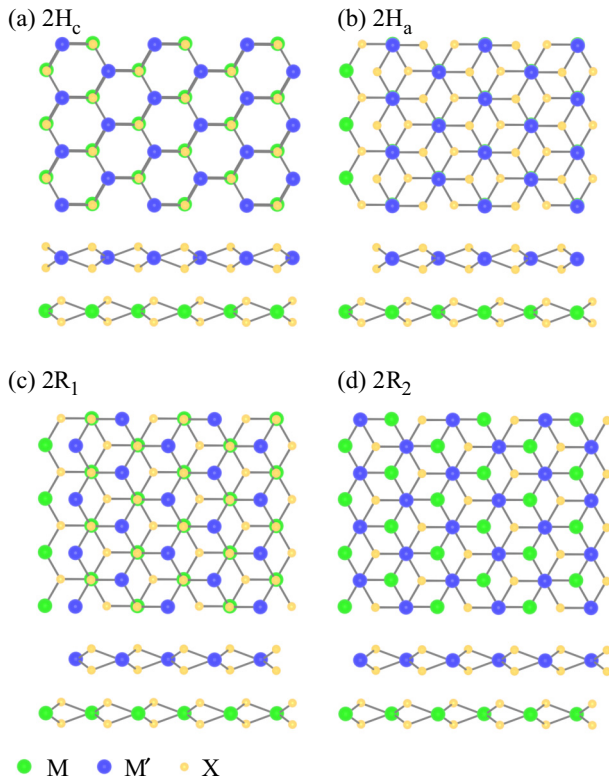

FIG. 2. Four highly symmetric stacking structures of two 1H TMDC monolayers. The top view and horizontal view of the stacking layers are shown schematically. The spheres represent transition atoms and chalcogen atoms, MX_2 and $M'X_2$ with M = Nb or Ta, M' = Mo or W, and X = S or Se.

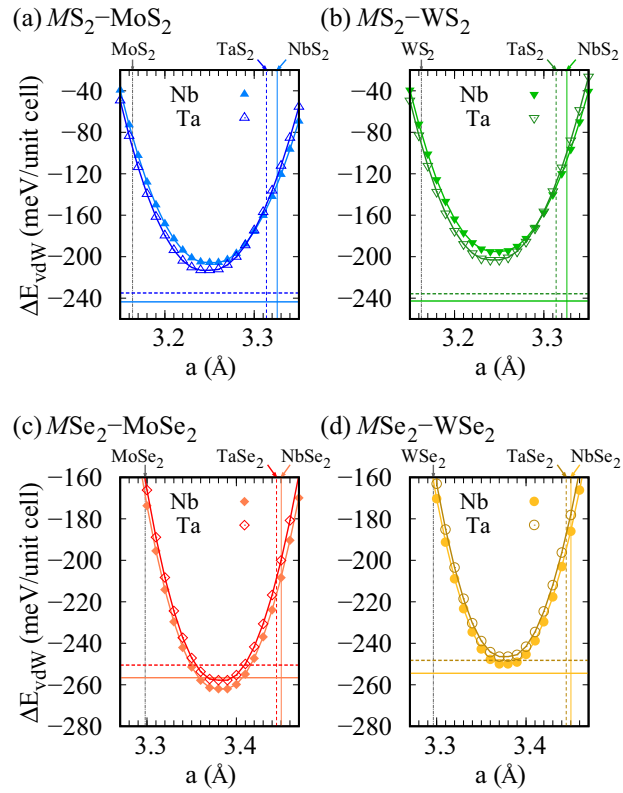

FIG. 3. Lattice constant dependence of electronic energy for $2R_2$ vdW heterobilayers. The filled and blank marks represent the heterobilayers with Nb and Ta as M, respectively. The solid and dashed horizontal lines denote the estimated energies of the moiré heterobilayers with Nb and Ta, respectively. The energy is given with respect to that of the two isolated monolayers. The vertical lines represent the lattice constants of pristine monolayers.

the spinless condition with the correction of vdW interaction because the spin-orbit coupling is much smaller than the vdW interaction in the interlayer interaction. The total electronic energy of each stacking structure in the optimized lattice is presented in Table I. For all cases, the heterobilayer possesses the lower energy than that of two isolated monolayers, i.e., it is more stable than two isolated monolayers, even if each layer is compressed or expended in the heterostructure. Moreover, $2R_2$ stacking structure gives the lowest energy for any combination of elements among the four structures.

TABLE I. The total electronic energies of vdW heterobilayers MX_2-MX_2 for four stacking structures. The energy is given in meV as the deviation from that of two isolated monolayers MX_2 and MX_2 with the optimized lattice constants. The upper and lower divisions are devoted to the sulfide layers and the selenide layers, respectively.

	NbS_2-MoS_2	NbS_2-WS_2	TaS_2-MoS_2	TaS_2-WS_2
$2H_c$	−192.0	−183.1	−201.5	−192.9
$2H_a$	−203.9	−190.7	−208.3	−196.0
$2R_1$	−201.1	−190.5	−207.6	−197.7
$2R_2$	−206.8	−195.2	−214.2	−203.2
	$NbSe_2$-$MoSe_2$	$NbSe_2$-WSe_2	$TaSe_2$-$MoSe_2$	$TaSe_2$-WSe_2
$2H_c$	−248.4	−239.4	−246.8	−238.0
$2H_a$	−253.8	−240.0	−246.6	−233.6
$2R_1$	−255.0	−243.0	−250.6	−239.0
$2R_2$	−262.1	−250.2	−258.0	−246.7

The stable stacking structure, $2R_2$, is different from the pristine metallic and semiconducting bilayers, $2H_a$ and $2H_c$, respectively. However, $2R_2$ stacking possesses the characteristics of both the metallic and semiconducting bilayers in terms of the configurations between transition-metal atoms and chalcogen atoms allocated in different component layers. In a pristine metallic (semiconducting) bilayer, the $2H_a$ ($2H_c$) structure maximizes (minimizes) the distance between the nearest transition-metal atom and chalcogen atom allocated in different component layers. In $2R_2$ stacking, a transition-metal atom in the metallic and semiconducting layers fulfills the above conditions simultaneously for the nearest chalcogen in the other layer. Thus the $2R_2$ stacking structure is preferable for both the metallic and semiconducting component layers in the vdW heterobilayer. Therefore, the most stable stacking structure, $2R_2$ stacking, is considered in the following investigations.

The lattice constant of the heterobilayer is almost in the middle between those of the isolated component layers and strongly depends on the species of chalcogen. In Fig. 3, the lattice constant dependence of the electronic energy for the $2R_2$ heterobilayer is presented. The maximum and minimum values in the horizontal axis are almost the lattice constants

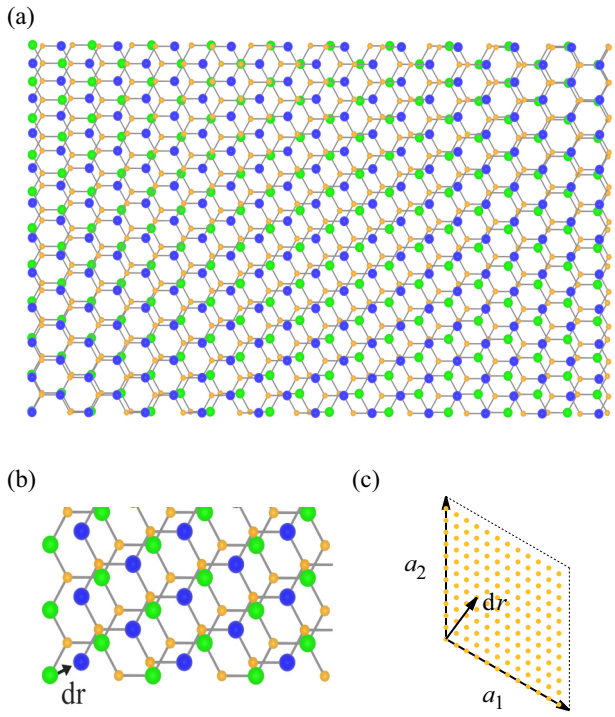

FIG. 4. Schematics of (a) a moiré structure and (b) a commensurate stacking with a displacement dr. In (c), the distribution of displacement vector dr is presented with the lattice vectors, $\boldsymbol{a}_1$ and $\boldsymbol{a}_2$.

of the pristine crystals of the metallic layer (NbX_2 or TaX_2) and semiconducting layer (MoX_2 or WX_2), respectively. The lattice constant giving the lowest energy is that of the $2R_2$ heterobilayer in the optimized lattice structure. The numerical results clearly show that the lattice constant of the heterobilayer is about the middle value between those of the two component layers. Therefore, both the component layers are compressed or extended from the pristine lattice structures in forming the heterobilayer.

Secondly, the commensurate vdW heterobilayer is compared with the moiré heterobilayer in terms of the total electronic energy. A moiré heterobilayer is produced by stacking two different monolayers and preserving their original lattice constants as shown in Fig. 4(a). In this heterostructure, each layer can preserve the lattice structure of pristine monolayer without any deformation. However, the local stacking structure is not the lowest-energy one, $2R_2$, and varies according to the location. In general, the first-principles calculation for a moiré structure is too difficult because it possesses a much larger periodicity than that of the original layers or no explicit periodic structure. In practice, the difference of lattice constants in $MoSe_2$ and $NbSe_2$ is about 5% and it requires 20 times the original lattice constant of a monolayer even if the difference is assumed to be 5% exactly. Thus an estimation is adopted for the calculation of the electronic energy in the moiré structure as follows:

$$E^{\text{moiré}} = \sum_M \left(E^0_{MX_2} - E'_{MX_2}\right) + \overline{E^{\text{bi}}(dr)}, \tag{1}$$

where $E^0_{MX_2}$ and E'_{MX_2} are the electronic energy for an isolated monolayer MX_2 with the pristine lattice constant and the lattice constant of the commensurate vdW heterostructure, respectively, and $\overline{E^{\text{bi}}(dr)}$ is the average energy of commensurate vdW heterobilayers with various displacements dr between two layers in Fig. 4(b). Here, dr is given by $(n_1\boldsymbol{a}_1 + n_2\boldsymbol{a}_2)/N$ with $0 \leqslant n_j < N$ for $N = 12$ as shown in Fig. 4(c).

In Fig. 3, the estimated electronic energy for the moiré structure is presented by a horizontal line for each heterobilayer MX_2-$M'X_2$.

Here, the energy for the moiré structure is also given with respect to the energy of isolated two component layers,

$$\Delta E^{\text{moiré}} = E^{\text{moiré}} - \sum_M E^0_{MX_2}, \tag{2}$$

to compete with ΔE_{vdW}.

For vdW heterobilayers of sulfides, the numerical results clearly show that the moiré heterobilayer gives a much lower energy than that of the commensurate heterobilayer as shown in Figs. 3(a) and 3(b). Thus the moiré structure can be more stable than the commensurate stacking structure and a feasible structure for any combination of transition-metal atoms. In the cases of selenides, on the other hand, the commensurate heterobilayer gives an electronic energy comparable to that for the moiré heterobilayer. Especially in the case of $MoSe_2$, the electronic energy for the commensurate structure is obviously lower than the estimated value for the moiré structure.

The numerical results clearly show that the commensurate stacking structure is more preferable for selenide layers to form the heterobilayer. The difference due to the chalcogen sublayers is attributed to an increase in the electronic energy for each component layer with a change of lattice constant from the pristine monolayer. In Fig. 5, the variation of electronic energy is presented for several isolated monolayers with several lattice constants. The origin in the x axis represents the optimized lattice constant for each commensurate heterobilayer MX_2-$M'X_2$. The electronic energy of the isolated monolayer is given with respect to that for the monolayer possessing the lattice constant of the heterobilayer. Here, the bottom of each curve denotes the electronic energy of the pristine monolayer. The numerical results indicate that each sulfide layer obtains a larger energy benefit than the selenide layer when relaxing to the pristine structure. Since the incommensurate heterobilayer consists of layers with the pristine lattice constant, the incommensurate structure is more preferable for sulfide heterobilayers. In other words, the commensurate heterostructure is more feasible for the heterobilayers of transition-metal diselenide monolayers.

III. ELECTRONIC STRUCTURE IN THE COMMENSURATE HETEROBILAYER

In heterostructures of TMDCs, the electronic structures are affected by not only vdW interaction but also spin-orbit coupling [33]. The band calculation is performed using QUANTUM ESPRESSO with a lattice structure given by a lattice optimization calculation. The effect of spin-orbit coupling can be included in first-principles calculations but it cannot be adopted concurrently with the correction for vdW interaction to the XC functional. Actually, the two effects are

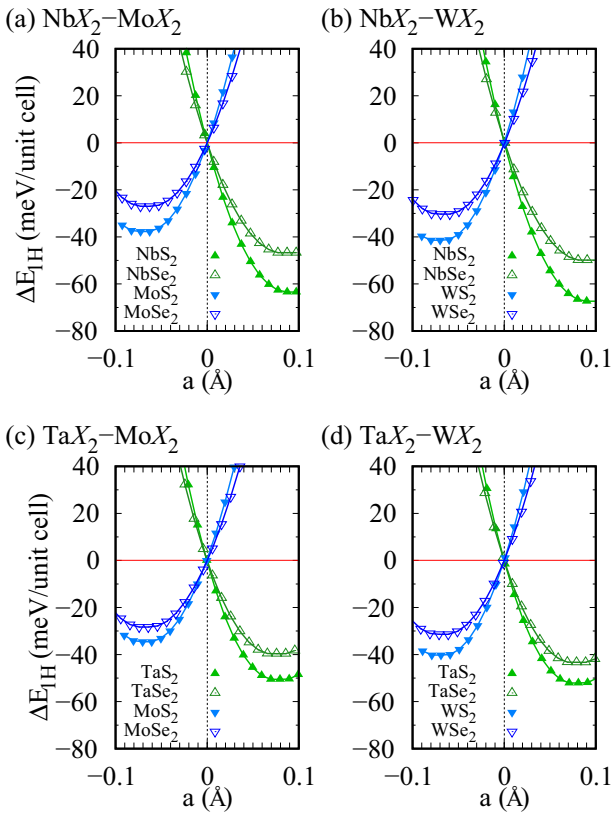

FIG. 5. Electronic energy of pristine monolayer TMDCs with several lattice constants. Each panel presents the numerical results for isolated monolayers included as the component layers in a heterobilayer $MX_2 - M'X_2$. The x axis represents the change of lattice constant from that of the heterobilayer. The electronic energy is represented with respect to that for the isolated monolayer with the lattice constant of the heterobilayer.

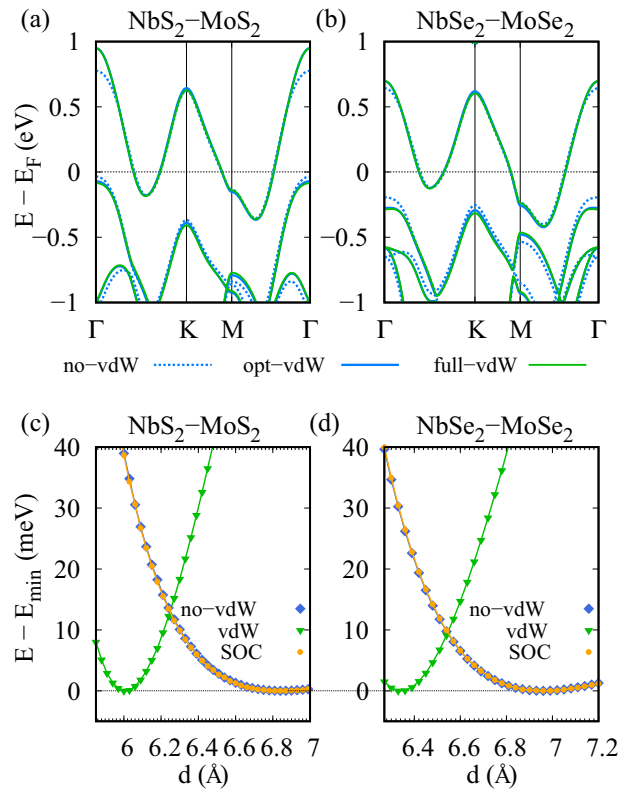

FIG. 6. Spinless band structures obtained under three different conditions of XC functional for (a) NbS_2-MoS_2 and (b) $NbSe_2$-$MoSe_2$. In (c) and (d), the total electronic energy is given for various interlayer distances.

not necessary in the same calculation process for obtaining a plausible band structure. The calculation is divided into two processes: the lattice optimization and the band calculation. In what follows, it is shown that vdW interaction and spin-orbit coupling are crucial only in the former and latter calculations, respectively.

First, the role of vdW interaction is investigated in the lattice optimization calculation and the band calculation for commensurate heterobilayers. In Figs. 6(a) and 6(b), the spinless band structures are presented under three different conditions on the correction for vdW interaction. The first condition (no-vdW) is to perform these calculations without the correction. The second condition (opt-vdW) is to apply the correction only to the lattice optimization. The third condition (full-vdW) is to adopted the correction in both the two calculations. The band structures with the lattice optimized with vdW interaction are almost the same regardless of the correction to the band calculation. On the other hand, the absence of the correction in the lattice optimization leads to a visible difference in the band structure. These numerical results clearly show that the correction plays a crucial role in optimizing the lattice structure but it has a minor contribution to the band calculation.

Next, the contribution of spin-orbit coupling is investigated in the lattice optimization. In Figs. 6(c) and 6(d), the total electronic energy is presented for various interlayer distances defined between transition-metal sublayers under different calculation conditions: the optimization with the correction for vdW interaction (vdW), that with spin-orbit coupling (SOC), and that without any correction (no-vdW). The distance for the lowest energy indicates that of the stable heterobilayer and it changes with the application of the correction for vdW interaction. However, spin-orbit coupling does not change the energy variation with the interlayer distance. Moreover, the lattice constant of honeycomb lattice is almost unchanged in the presence of spin-orbit coupling. The other heterobilayers, MX_2-$M'X_2$, also show similar relations among the conditions in each calculation process. Therefore, a plausible band structure for the heterobilayer can be given by the first-principles band calculation with spin-orbit coupling in the lattice structure optimized with vdW interaction.

A. Heterobilayer of sulfide layers

In Fig. 7, the electronic and spin structures of commensurate $2R_2$ heterobilayers MS_2-$M'S_2$ are presented with the wave amplitudes for spin and layer degrees of freedom. The amplitudes are given by those on appropriate spinful Wannier orbitals calculated using WANNIER90 [34], a code to give maximally localized Wannier orbitals and hopping integrals among the orbitals from a first-principles band structure. Five

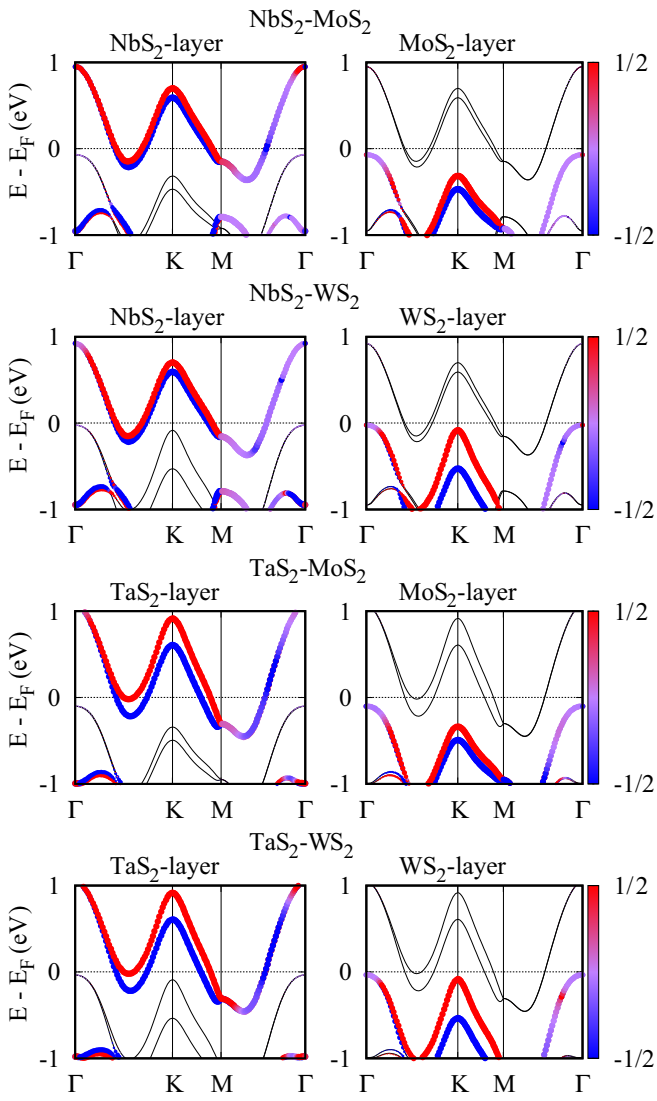

FIG. 7. Spinful band structures with the amplitudes of spin and layer degrees of freedom for MS$_2$-M'S$_2$. The size and color of mark represent the amplitudes of wave function and spin polarization in the perpendicular direction to the layers.

d orbitals in a transition-metal atom and six p orbitals in two chalcogen atoms are adopted as the Wannier orbitals for each layer in the unit cell. Thus a tight-binding model is obtained using the hopping integrals defined on the 44 spinful Wannier orbitals and it provides wave functions represented by wave amplitudes on the orbitals. Especially on the M-Γ line, the spin amplitude shows irregular variations but it is artifacts of numerical calculations due to the almost degenerated spin states.

In every case, a single partially filled band and a fully filled band can be found around the Fermi energy. The partially filled band fully consists of Wannier orbitals in the metallic layer, NbS$_2$ or TaS$_2$, and shows the dispersion similar to that in the pristine monolayer. The band possesses three local maxima at the Γ, K, and K' points and it provides two Fermi pockets around each of the high-symmetry points, so-called valleys, even though the metallic layer is deformed due to the formation of the heterobilayer. Here, time-reversal symmetry promises the same dispersion with the inverted spin in the K and K' valleys. In the two valleys, the spin states are split due to spin-orbit coupling in the spin axis along the perpendicular direction to the layers and the order of spin states is inverted due to time-reversal symmetry.

The highest fully filled band consists of Wannier orbitals in the semiconducting layer, MoS$_2$ or WS$_2$, but the structure is different from that in the monolayer material. Although the maximum electronic energy in the monolayer appear at the K point (and the K' point), the energy at the K point is lower than that at the Γ point in the cases of heterobilayers. This is the characteristic feature of bilayer materials [35,36] but the spin split at the K point is the same as the monolayer. Therefore, in the heterobilayer of sulfide layers, the highest fully filled band is composed of Wannier orbitals in the semiconducting layer and obtains the characteristics of both the monolayer and bilayer materials.

B. Heterobilayer of selenide layers

The electronic and spin structures for selenide heterobilayers MSe$_2$-M'Se$_2$ are presented in Fig. 8. These band structures are similar to those for sulfide heterobilayers in terms of the partially filled band. In the partially filled band, electronic states consist of Wannier orbitals localized in the metallic layer and show a spin split in the K and K' valleys. For the bilayers of Ta, however, the Fermi pockets are not isolated in three valleys because the upper branch does not cross the Fermi level as shown in the lower four panels of Fig. 8. On the other hand, the highest fully filled band possesses different features in the dispersion from that for sulfide heterobilayers. The maximum energy state appears at the K (K') point and the electronic states around the Γ point are constructed of orbitals in both the metallic and semiconducting layers. Moreover, the numerical results indicate the presence of conductive states in the WSe$_2$ layer, i.e., the Fermi energy is lower than the top of the band for the NbSe$_2$-WSe$_2$ heterobilayer. The conductive states indicate the charge transfer between the metallic and semiconducting layers. The charge transfer is absent in the cases of MSe$_2$-MoSe$_2$, but the TaSe$_2$-WSe$_2$ heterobilayers possess electronic energy states close to the Fermi energy in this band. Thus thermally excited charge can appear in the band around the K and K' points even at a low temperature. For MSe$_2$-MoSe$_2$ heterobilayers, the excitation energy between a filled band and the Fermi energy is more than 200 meV and thus it indicates that the semiconducting layer can be an insulating cover or substrate for the metallic layer. In the heterobilayers composed of a unique chalcogenide, the charge transfer is suppressed between the metallic and semiconducting layers but it is in contrast to similar heterobilayers of NbS$_2$-M'Se$_2$ for M' = Mo or W in a previous work [27]. In the previous work, a large number of charges is theoretically predicted to transfer to the semiconducting layer as shown in Fig. 9. Since the previous work also shows the $2R_2$ stacking to be the most stable structure for NbS$_2$-MoSe$_2$ and NbS$_2$-WSe$_2$, the obvious difference is that different chalcogen sublayers—sulfur and selenide sublayers—are adopted in the metallic and semiconducting layers, respectively. Thus the chalcogen

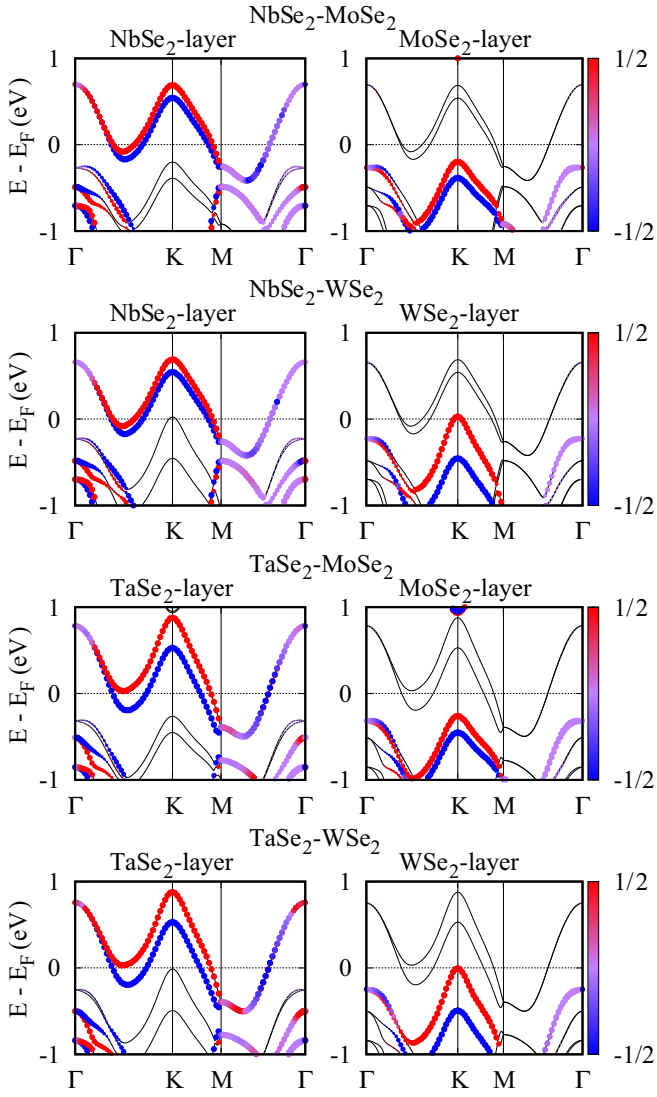

FIG. 8. Spinful band structures with the amplitudes of spin and layer degrees of freedom for $M\mathrm{Se}_2$-$M'\mathrm{Se}_2$. The left and right columns show the wave amplitude in the metallic and semiconducting layers, respectively, represented by the size of marks. The spin polarization is also represented by the color.

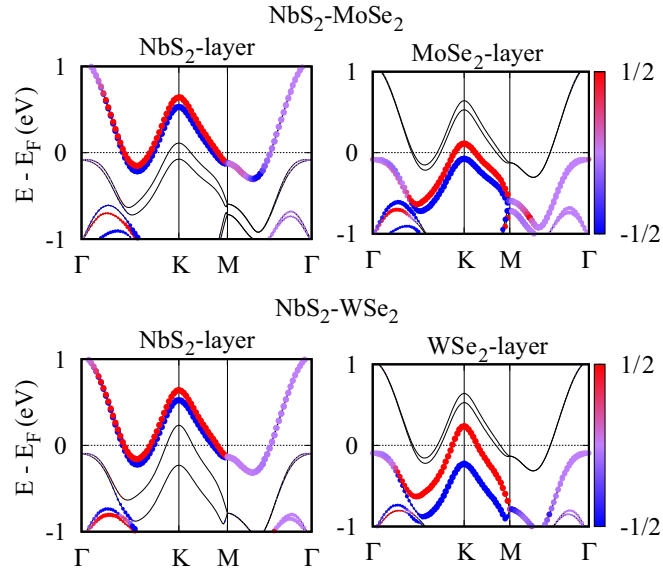

FIG. 9. Spinful band structures with the amplitudes of spin and layer degrees of freedom for vdW heterobilayer of NbS_2 and semiconducting transition-metal diselenide. The size and color of marks represent the amplitude in a component layer and the spin polarization. The left and right panels show the amplitude for the NbS_2 layer and semiconducting layer, respectively.

sublayers dominate the charge transfer between the metallic and semiconducting layers in the heterostructure.

Charge transfer at an interface of two materials is, in general, attributed to the difference of work functions, which is defined by the difference between the highest energy of occupied states and vacuum level, in the two materials. In Fig. 10, the electrostatic potential profile around a pristine monolayer and the highest energy of occupied states are presented for the component layers in this work. The potential is averaged in the xy plane parallel to the layer and drawn in the normal axis to the layer. The numerical calculation is performed in a periodic boundary condition with a spacer 30 Å between adjacent layers, where the transition-metal sublayer is placed at the origin in the horizontal axis. The electrostatic potential is fluctuated around the origin but it approaches a unique value except for the vicinity of the layer. Since the potential far from the layer provides vacuum level E_∞, the excitation energy to E_∞ from the highest energy of occupied states gives the work function. In Fig. 10, the highest energy of occupied states is represented by a horizontal line and the distance from the origin, $E - E_\infty = 0$, is equal to the work function.

In the pristine monolayers, the work function is affected by the chalcogen rather than the transition-metal as shown in Fig. 10. In fact, the highest energy of occupied states is comparable among sulfide monolayers or selenide monolayers with respect to vacuum level but the change of chalcogen leads to a visible variation in the energy. In Table II, the numerical results of work function W_X are presented for the pristine monolayers MX_2 for $X = \mathrm{S}$ and Se. Moreover, the work functions are also given for the monolayer crystals with the lattice constant adjusting to that of the heterobilayer, e.g., NbS_2-MoS_2 and TaS_2-MoS_2 in the case of MoS_2 monolayer, and the average W'_X for the lattice constants is also presented in Table II. Obviously, the deviation of work function among the monolayers decreases with adjusting the lattice constant to that of the heterobilayer for each chalcogen X. Thus, in

TABLE II. Work functions of monolayer MX_2 with the pristine lattice constant W_X and that of $2R_2$ heterobilayers W_X. Here, W_X is the averaged value over heterobilayers of different partners. These energies are given in the unit of eV.

	$\mathrm{Nb}X_2$	$\mathrm{Mo}X_2$	$\mathrm{Ta}X_2$	$\mathrm{W}X_2$
W_S	6.062	5.845	5.891	5.471
W'_S	5.977(2)	5.975(2)	5.821(2)	5.577(2)
W_Se	5.476	5.159	5.300	4.793
W'_Se	5.388(2)	5.274(3)	5.217(3)	4.881(2)

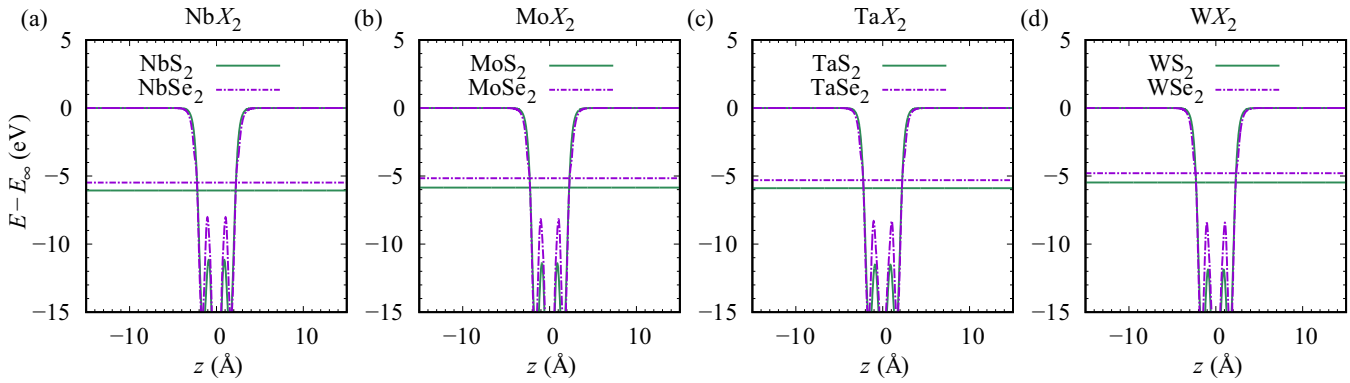

FIG. 10. Averaged electrostatic potentials for pristine monolayers: (a) NbX_2, (b) MoX_2, (c) TaX_2, and (d) WX_2 for X = S and Se. The horizontal axis indicates the position in the normal axis to the layer with respect to the transition-metal sublayer. The vertical axis represents the potential in eV with respect to the vacuum level E_∞. Each horizontal line represents the highest energy of occupied states.

the heterobilayer, the metallic and semiconducting component layers possess similar work functions. The comparable work functions suppress a charge transfer between two layers in heterobilayers except for the tungsten layer. In the case of a layer with tungsten, the work function is much lower than those of the other monolayers. Thus a small charge transfer is indicated for heterobilayer $NbSe_2$-WSe_2. The large difference of the work function between the sulfide and selenide layers also provides a clear understanding of a large charge transfer for NbS_2-$MoSe_2$, a heterostructure of monolayers with different chalcogen sublayers, in a previous work [27].

IV. CONCLUSION

We have investigated the crystal and electronic structures of a commensurate vdW heterobilayer composed of metallic and semiconducting TMDC monolayers with the same chalcogen and revealed two important roles of chalcogen sublayers: stabilizing the commensurate heterostructure and controlling the charge transfer between metallic and semiconducting layers. First-principles calculations reveal that $2R_2$ stacking gives the lowest ground-state energy for the commensurate heterobilayers among various stacking structures and it is more stable than two isolated pristine monolayers due to the vdW interaction in the heterobilayers. Moreover, it is shown that selenide sublayers make vdW heterobilayers comparably or more stable in comparison with the moiré bilayer. In the $2R_2$ vdW heterobilayers, electronic states in a partially filled band are fully localized in the metallic layer and those in the highest band below the partially occupied one are almost occupied. The electronic structure indicates the absence of a large charge transfer between two layers in contrast to the case of NbS_2-$MoSe_2$ (WSe_2) heterobilayer in Ref. [27]. First-principles calculations have shown that the work function of each layer strongly depends on the chalcogen sublayers and it is comparable between the two component layers with the same chalcogen. These theoretical results suggest that the chalcogen sublayers play a crucial role in metal-semiconductor vdW heterostructure of TMDC monolayers.

ACKNOWLEDGMENT

This work was supported by Japanese Society for the Promotion of Science (JSPS) KAKENHI Grant No. JP23K03289.

[1] R. Kershaw, M. Vlasse, and A. Wold, Inorg. Chem. **6**, 1599 (1967).
[2] M. Naito and S. Tanaka, J. Phys. Soc. Jpn. **51**, 219 (1982).
[3] D. Xiao, G.-B. Liu, W. Feng, X. Xu, and W. Yao, Phys. Rev. Lett. **108**, 196802 (2012).
[4] Q. H. Wang, K. Kalantar-Zadeh, A. Kis, J. N. Coleman, and M. S. Strano, Nat. Nanotechnol. **7**, 699 (2012).
[5] E. Cappelluti, R. Roldán, J. A. Silva-Guillén, P. Ordejón, and F. Guinea, Phys. Rev. B **88**, 075409 (2013).
[6] G.-B. Liu, W.-Y. Shan, Y. Yao, W. Yao, and D. Xiao, Phys. Rev. B **88**, 085433 (2013).
[7] S. Helveg, J. V. Lauritsen, E. Lægsgaard, I. Stensgaard, J. K. Nørskov, B. S. Clausen, H. Topsøe, and F. Besenbacher, Phys. Rev. Lett. **84**, 951 (2000).
[8] A.-Y. Lu, H. Zhu, J. Xiao, C.-P. Chuu, Y. Han, M.-H. Chiu, C.-C. Cheng, C.-W. Yang, K.-H. Wei, Y. Yang, Y. Wang, D. Sokaras, D. Nordlund, P. Yang, D. A. Muller, M.-Y. Chou, X. Zhang, and L.-J. Li, Nat. Nanotechnol. **12**, 744 (2017).
[9] J. Zhang, S. Jia, I. Kholmanov, L. Dong, D. Er, W. Chen, H. Guo, Z. Jin, V. B. Shenoy, L. Shi, and J. Lou, ACS Nano **11**, 8192 (2017).
[10] A. K. Geim and I. V. Grigorieva, Nature (London) **499**, 419 (2013).
[11] K. S. Novoselov, A. Mishchenko, A. Carvalho, and A. H. C. Neto, Science **353**, aac9439 (2016).
[12] Y. Liu, N. O. Weiss, X. Duan, H.-C. Cheng, Y. Huang, and X. Duan, Nat. Rev. Mater. **1**, 16042 (2016).
[13] T. Deilmann, M. Rohlfing, and U. Wurstbauer, J. Phys.: Condens. Matter **32**, 333002 (2020).
[14] Z. Gong, G.-B. Liu, H. Yu, D. Xiao, X. Cui, X. Xu, and W. Yao, Nat. Commun. **4**, 2053 (2013).

[15] M. Sharma, A. Kumar, P. K. Ahluwalia, and R. Pandey, J. Appl. Phys. **116**, 063711 (2014).
[16] R. Bistritzer and A. H. MacDonald, Proc. Natl. Acad. Sci. USA **108**, 12233 (2011).
[17] R. Bistritzer and A. H. MacDonald, Phys. Rev. B **84**, 035440 (2011).
[18] T. Li, S. Jiang, L. Li, Y. Zhang, K. Kang, J. Zhu, K. Watanabe, T. Taniguchi, D. Chowdhury, L. Fu, J. Shan, and K. F. Mak, Nature (London) **597**, 350 (2021).
[19] K. F. Mak and J. Shan, Nat. Nanotechnol. **17**, 686 (2022).
[20] Y. Zhang, L. Yin, J. Chu, T. A. Shifa, J. Xia, F. Wang, Y. Wen, X. Zhan, Z. Wang, and J. He, Adv. Mater. **30**, 1803665 (2018).
[21] T. Habe, J. Appl. Phys. **126**, 123901 (2019).
[22] T. Habe, Phys. Rev. B **100**, 165431 (2019).
[23] P. Kumari, Z. Golsanamlou, A. Smogunov, L. Sementa, and A. Fortunelli, Phys. Rev. B **108**, 075404 (2023).
[24] Q. Fu, X. Wang, J. Zhou, J. Xia, Q. Zeng, D. Lv, C. Zhu, X. Wang, Y. Shen, X. Li, Y. Hua, F. Liu, Z. Shen, C. Jin, and Z. Liu, Chem. Mater. **30**, 4001 (2018).
[25] A. L. M. T. Costa, F. W. N. Silva, and E. B. Barros, Semicond. Sci. Technol. **33**, 075018 (2018).
[26] Z. Golsanamlou, P. Kumari, L. Sementa, T. Cusati, G. Iannaccone, and A. Fortunelli, Adv. Electron. Mater. **8**, 2200020 (2022).
[27] T. Habe, Phys. Rev. B **107**, L241404 (2023).
[28] P. Giannozzi, S. Baroni, N. Bonini, M. Calandra, R. Car, C. Cavazzoni, D. Ceresoli, G. L. Chiarotti, M. Cococcioni, I. Dabo, A. Dal Corso, S. de Gironcoli, S. Fabris, G. Fratesi, R. Gebauer, U. Gerstmann, C. Gougoussis, A. Kokalj, M. Lazzeri, L. Martin-Samos *et al.*, J. Phys.: Condens. Matter **21**, 395502 (2009).
[29] J. P. Perdew, K. Burke, and M. Ernzerhof, Phys. Rev. Lett. **77**, 3865 (1996).
[30] K. Berland, D. Chakraborty, and T. Thonhauser, Phys. Rev. B **99**, 195418 (2019).
[31] T. Thonhauser, V. R. Cooper, S. Li, A. Puzder, P. Hyldgaard, and D. C. Langreth, Phys. Rev. B **76**, 125112 (2007).
[32] R. Sabatini, E. Küçükbenli, B. Kolb, T. Thonhauser, and S. de Gironcoli, J. Phys.: Condens. Matter **24**, 424209 (2012).
[33] L. Sun, J. Yan, D. Zhan, L. Liu, H. Hu, H. Li, B. K. Tay, J.-L. Kuo, C.-C. Huang, D. W. Hewak, P. S. Lee, and Z. X. Shen, Phys. Rev. Lett. **111**, 126801 (2013).
[34] A. A. Mostofi, J. R. Yates, Y.-S. Lee, I. Souza, D. Vanderbilt, and N. Marzari, Comput. Phys. Commun. **178**, 685 (2008).
[35] W. Jin, P.-C. Yeh, N. Zaki, D. Zhang, J. T. Sadowski, A. Al-Mahboob, A. M. van der Zande, D. A. Chenet, J. I. Dadap, I. P. Herman, P. Sutter, J. Hone, and R. M. Osgood, Phys. Rev. Lett. **111**, 106801 (2013).
[36] J. He, K. Hummer, and C. Franchini, Phys. Rev. B **89**, 075409 (2014).